ADVANCED ENERGY MATERIALS
www.advenergymat.de

1D Stretchable Block Copolymer Yarn-Based Energy Harvesters via $BaTiO_3$/Polydimethylsiloxane Composite-Carbon Conductive Ink

*Jaeho Kim, Woojong Kim, Gabriel Jang, Da Seul Hyeon, Mi Hyun Park, and Jin Pyo Hong**

Highly stretchable self-powered energy sources are promising options for powering diverse wearable smart electronics. However, commercially existing energy sources are disadvantaged by tensile strain limitations and constrained deformability. Here, 1D thread-based highly stretchable triboelectric nanogenerators (HS-TENGs), a crucial step toward overcoming these obstacles, are developed based on a highly stretchable coaxial-type poly[styrene-*b*-isoprene-*b*-styrene] (SIS) elastomer tube. Carbon conductive ink is injected into the SIS tube as a core 1D electrode that remains almost unaffected even under 250% stretching because of its low Young's modulus. To further facilitate power generation by the HS-TENG, a composite of barium titanate nanoparticles ($BaTiO_3$ NPs) and polydimethylsiloxane (PDMS) is coated on the initial SIS tube to modulate the dielectric permittivity based on variations in the $BaTiO_3$ NPs volume ratio. The 1D PDMS/$BaTiO_3$ NP composite-coated SIS and a nylon 6-coated 2D Ni–Cu conductive fabric are selected as triboelectric bottom and top layers, respectively. Woven HS-TENGs textiles yield consistent power output under various extreme and harsh conditions, including folded, twisted, and washed states. These experimental findings indicate that the approach may become useful for realizing stretchable multifunctional power sources for various wearable electronics.

1. Introduction

Recently developed advanced portable and wearable electronics strongly require reliable and independent power sources to extend their enormous potential.[1,2] However, the widespread utilization of conventionally available energy supplies like batteries or supercapacitors is challenging because of their inherent limitations in shape and deformability. To address this, self-powered energy harvesters have emerged as sustainable, reliable, and maintenance-free alternatives, converting abundant mechanical energy resources in the living environment of human motion into electricity to power wearable devices.[3,4] Many reports investigating electromagnetic, piezoelectric, and pyroelectric materials toward energy harvesting in daily life have been published.[5–11] Among the developed candidates, triboelectric nanogenerators (TENG) based on the charge transfer-driven coupling interaction of the triboelectric effect and electrostatic induction are considered the most promising self-power sources for harvesting energy produced by various human body motions.[12–16]

To date, many works have focused on exploiting triboelectric self-powered energy sources based on 2D wearable textile or fabric platforms.[17–23] As examples, Seung et al. reported the performance of a fully flexible and foldable nanopatterned wearable TENG using ZnO nanorod arrays on an Ag-coated textile template.[24] Wang et al. also reported on stretchable, flexible, and wearable TENGs in the form of kinesio-tape, thus demonstrating successful operation as active human motion-sensing devices.[25] However, these 2D textile- or fabric-based TENGs still provide insufficient degrees of freedom in geometric parameters such as tensile strain and deformability, thus restricting the realization of wearable electronics. In this regard, solving these issues of wearable TENGs is critical for the widespread implementation of diverse applications including stretchable electrodes; human motion sensors; and energy conversion, management, and storage.[26]

Here we report the performance of a 1D thread-based highly stretchable TENG (HS-TENG) based on a 1D poly[styrene-*b*-isoprene-*b*-styrene] (SIS) tube as a unique template allowing a stretchable and coaxial configuration. Carbon conductive ink (CCI) comprising carbon, graphite, and synthetic oil is employed as a core conductive electrode of the HS-TENG through an injection approach. Polydimethylsiloxane (PDMS) engineered with suitable $BaTiO_3$ nanoparticle (NP) loading on the 1D SIS and 2D nylon 6-coated conductive Ni–Cu fabric are chosen as the bottom and top plates for measurement, respectively, because of the effective charge transfer induced

J. Kim, W. Kim, M. H. Park, Prof. J. P. Hong
Division of Nano-Scale Semiconductor Engineering
Hanyang University
Seoul 04763, South Korea
E-mail: jphong@hanyang.ac.kr
G. Jang, D. S. Hyeon, Prof. J. P. Hong
Research Institute for Natural Science
Department of Physics
Hanyang University
Seoul 04763, South Korea
The ORCID identification number(s) for the author(s) of this article can be found under https://doi.org/10.1002/aenm.201903217.

DOI: 10.1002/aenm.201903217

by the large polarity difference between these paired materials upon the contact–release process according to the triboelectric series.[27] As a critical modulation of the dielectric permittivity of the bottom PDMS-based plate to promote additional friction, $BaTiO_3$ NPs are systematically added to the PDMS layer by mixing. The optimized HS-TENG including the bottom PDMS layer engineered with 40 vol% $BaTiO_3$ NPs provides suitable performance under a compressive force of 34 N, with the output open-circuit voltage (V_{OC}), short-circuit current (I_{SC}), and power density of 76.8 V, 7.86 μA, and 200.9 μW cm^{-2}, respectively. The mechanically and electrically robust features of the HS-TENG are unaffected up to 250% elongation. To examine the potential integration of the HS-TENG into 2D or 3D fabric-based components, HS-TENG textiles prepared by weaving are tested to demonstrate their utility as sustainable power sources. This application to wearable electronic devices through energy harvesting from human body motion is presented with more detailed characterization under preirregular and less uniform harsh test conditions.

2. Results and Discussions

Figure 1 illustrates the fabrication of the 2D nylon 6-coated Ni–Cu fabric and highly stretchable 1D coaxial conductive threads (HS 1D-CCT) serving as top (positive) and bottom (negative) plates, respectively. In this work, a nylon 6-coated Ni-Cu fabric was chosen only to verify the influence of HS-TENG on the output performance and to exclude possible disadvantages of introducing unintended variables. A typical optical image of the large-size Ni–Cu textile substrate is given in the left of Figure 1a, and a magnified field-emission scanning electron microscopy (FE-SEM) image of the substrate is shown at the right of Figure 1a. As a top plate, nylon 6 is spin-coated as a full cover on the bare Ni–Cu fabric, which has a natural roughness. The right side of Figure 1a exhibits the FE-SEM image of 2D nylon 6-coated Ni–Cu fabric, revealing the microscale surface roughness induced by the introduction of a suitable hexane solvent during preparation. Figure 1b displays the schematic of fabrication for the bottom layer. First, the SIS elastomer is coated on a metal thread as a sacrificial buffer layer for a uniform PDMS coating on the metal thread via the thermal extrusion process, which can roughly allow for the semi-automatic continuous manufacturing steps (Figure S1, Supporting Information).[28] Direct PDMS coating of the metal thread causes the formation of nonuniform small droplets over the entire 1D surface, possibly from Plateau–Rayleigh instability (Figure S2a, Supporting Information).[29] $BaTiO_3$ NPs are added to the PDMS-coated SIS layer via dip coating, yielding a layer henceforth referred to as the PDMS/$BaTiO_3$ NP composite for convenience. After natural solidification at room temperature, the sacrificial metal thread is easily peeled from the cured PDMS/$BaTiO_3$ NP composite because of the inherently poor adhesion between these materials. Second, CCI is injected into the PDMS/$BaTiO_3$ NP-coated SIS tube by a syringe needle; the CCI comprises carbon, graphite, and synthetic oil. Finally, each HS 1D-CCT is precisely sealed with an external conductive Cu lead through a thermal compression method for electrical connection. A detailed discussion of each plate fabrication process is given in the Experimental Section. Figure S3a in the Supporting Information provides a representative cross-sectional optical image of the PDMS/$BaTiO_3$ NP composite coating on the coaxial SIS tube after the CCI injection as the core conductive electrode; the complete composite is denoted as HS 1D-CCT here. Each HS 1D-CCT with a diameter of ≈1.15 mm on average (Figure S3b, Supporting Information) is assembled in an array of ten as the negative bottom layer. Figure S3c–e in the Supporting Information present digital optical images

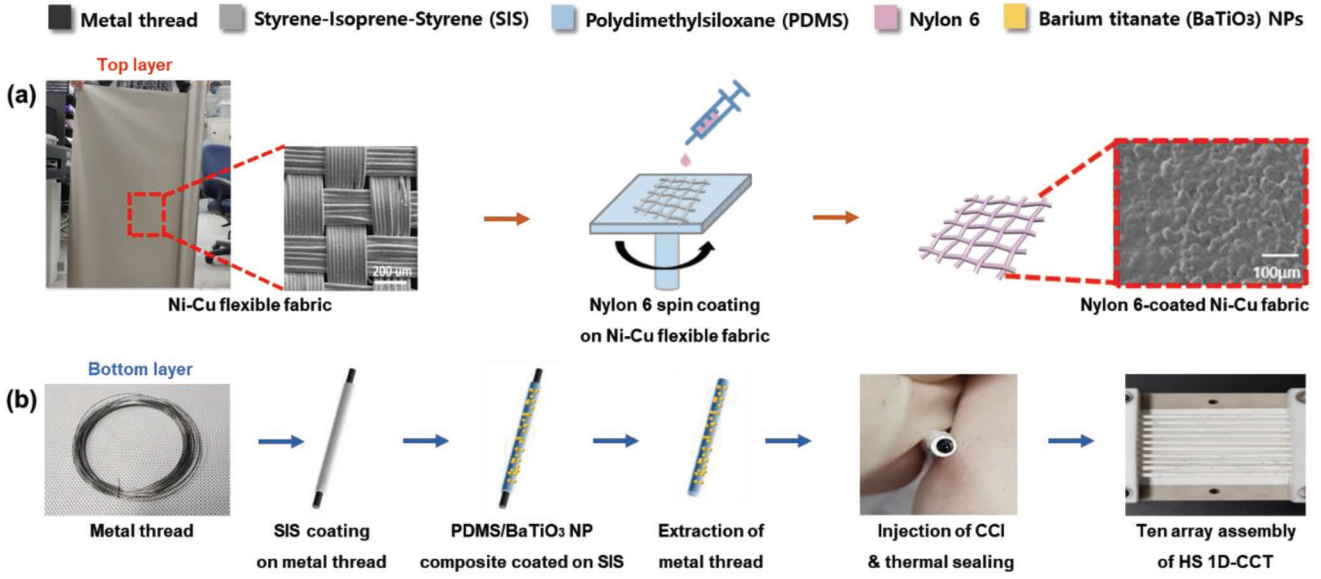

Figure 1. Schematic of the fabrication of HS-TENG: a) 2D nylon 6-coated Ni–Cu flexible fabric working as the top (positive) plate and b) highly stretchable (HS) 1D coaxial conductive threads (CCT) serving as the bottom (negative) plate, where the PDMS/$BaTiO_3$ nanoparticle (NP) composites are coated on the SIS layer through a dipping approach, followed by the injection of the carbon conductive ink (CCI) as the conductive electrode for the HS 1D-CCT. Ten HS 1D-CCTs are included in an array for electrical analysis.

of the ten-thread arrays of HS 1D-CCTs with only SIS, PDMS-coated SIS, and PDMS/$BaTiO_3$ NP composite-coated SIS. The HS-TENGs for electrical analysis comprise 2D nylon 6-coated Ni–Cu fabric (top electrode) and ten-thread HS 1D-CCT arrays (negative electrode). Additional cross-sectional photographs of only the SIS tube and the PDMS-coated SIS layers are given in Figure S4a,b in the Supporting Information for comparison.

To gain insight into the electrical and mechanical characteristics of the HS 1D-CCT component of the HS-TENG under various strain conditions, the electrical resistance and stretchable features of the HS 1D-CCT itself are tested in the range 0–250%, where the initial length of the HS 1D-CCT is 10 cm. **Figure 2**a reveals highly robust stretchable properties of the HS 1D-CCT up to 250%, together with a gradual decrease in the brightness of commercial green light emitting diode (LED) bulbs with increasing applied tensile strain. Figure 2b plots the variation in the normalized resistance of the HS 1D-CCT as a function of strain, demonstrating the negligible difference between the experimental and theoretical normalized resistance. The normalized resistance varies from 1 to 12.26 (Figure 2b). The increase in resistance with strain is likely linked to the gradual decrease in the cross-sectional area of the HS 1D-CCTs. Although the length of the HS 1D-CCT changes with the applied strain, the overall volume of CCI remains constant. The resistance increase of the HS 1D-CCT does not significantly affect the corresponding electrical output performance, except for a slight reduction in the output performance caused by the reduced surface contact areas during device operation, as described later. The stretching durability of the HS 1D-CCT is tested by consecutive repeated strain to 100%, as plotted in Figure 2c. As evident, the resistance of the HS 1D-CCT is almost unaffected over ≈7000 cycles of 100% consecutive stretching and releasing states, thus confirming the applicability of the SIS tube-based HS 1D-CCT as a basic platform for stretchable and wearable energy harvesters. In addition, uniaxial tensile analyses were conducted on the HS 1D-CCT itself (Figure S5, Supporting Information). For example, the HS 1D-CCT including the PDMS/$BaTiO_3$ NP composite (40 vol%) reveals the maximum strain of 518% at a stress of 0.53 MPa, while the HS 1D-CCT containing only PDMS shows the maximum strain of 913% at 0.52 MPa. The bare SIS-based HS 1D-CCT shows the best stretching properties, reaching 1624% at the stress of 2.01 MPa.

Figure 3 depicts the working mechanism of the HS-TENG under vertical-contact mode. No charge transfer is induced before the contact of the two plates in the initial state, which provides no electrical potential. Contact represents

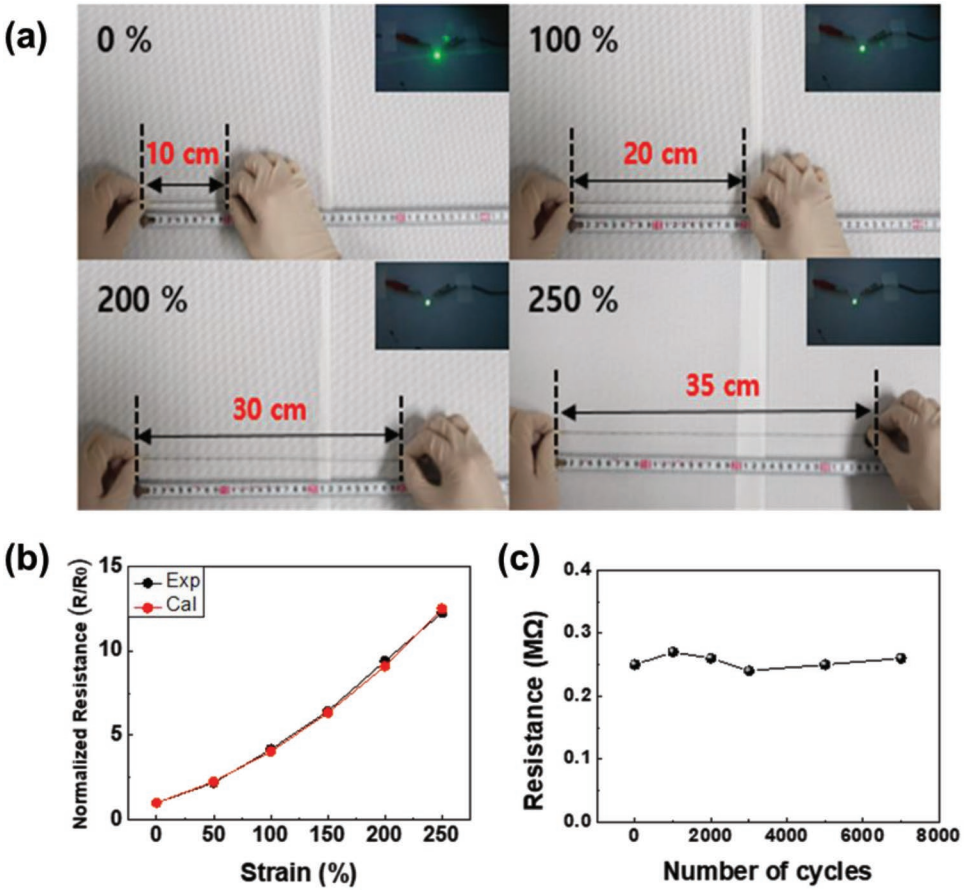

Figure 2. a) Optical images of HS 1D-CCT at initial and various stretched states, where insets indicate the demonstration of commercially available LED light bulbs operated at various tensile strains, thus reflecting the HS 1D-CCT's function as a conductive electrode. b) Strain-dependent experimental (black dots) and theoretical (red dots) resistances of the HS 1D-CCT. c) Variations in resistance of the HS 1D-CCT under 7000 repeated stretching–release cycles to 100% strain.

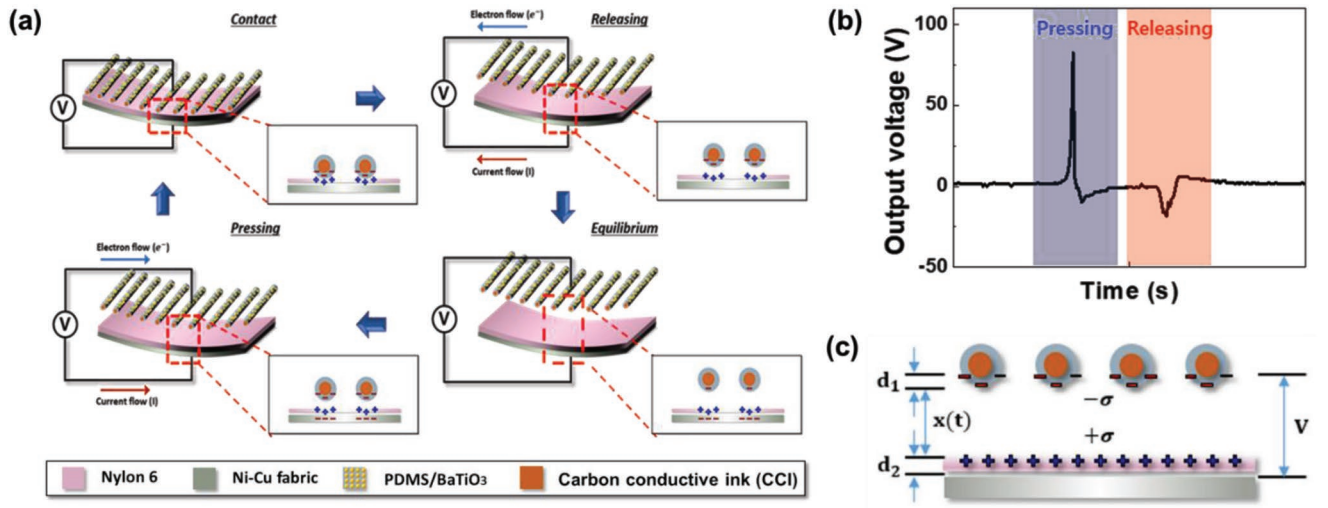

Figure 3. Operational principle of the HS-TENG. a) Schematic of the work mechanism of the HS-TENG under open-circuit conditions during repeated contact–separation processes. b) Representative single output voltage signal in one contact–separation process. c) Cross-sectional image of the HS-TENG with possible surface charge density.

the coincidence of the Fermi levels of the two materials, arising from charge exchange between the HS 1D-CCT and nylon 6;[30] in other words, an external force on the HS-TENG breaks the electrostatic equilibrium, thereby inducing electron transfer from the top to bottom electrodes. This is followed by the generation of a positive current through the external circuit. The absence of an external force is linked to the separation of the two triboelectric electrodes by their inherent elasticity. Consequently, the positive charges in the top electrode are neutralized with the transfer of electrons from the bottom electrode via the external circuit.[31,32] Figure 3a,b depicts the details of charge distribution under the vertical contact and release states and the corresponding output voltage in a single pressing–releasing cycle, respectively. Figure 3c presents a simple cross-sectional view of the HS-TENG, where the output voltage is described by adopting the following modified equation[33]

$$V_{oc} = \frac{\sigma}{\varepsilon_0}\left(\frac{2x}{l} + \frac{x^2}{l^2}\right)\left(\frac{d_1}{\varepsilon_{r1}} + \frac{d_2}{\varepsilon_{r2}}\right) \quad (1)$$

In Equation (1), ε_0, ε_{r1}, ε_{r2}, and σ are the vacuum permittivity, relative permittivity of PDMS (ε_{r1} = 2.8), relative permittivity of Nylon 6 (ε_{r2} = 3.6) and triboelectric charge density on elastomers, respectively, and l, x, d_1, and d_2 are the major axis of the contacting intersection, separation distance, thickness of PDMS, and thickness of nylon 6. More details of Equation (1) are given in Figure S6 in the Supporting Information. The incorporation of $BaTiO_3$ NPs in the PDMS is intended to provide a particular enhancement in the output performance. Considering Equation (1), the output voltage depends on σ, which is determined by the capacitance of the device in the vertical-contact mode of the HS-TENG. The maximum capacitance (C_{max}) of the device is given as follows[34]

$$C_{max} = \varepsilon_0 S \frac{\varepsilon_{r1}\varepsilon_{r2}}{d_1\varepsilon_{r2} + d_2\varepsilon_{r1}} \quad (2)$$

In Equation (2), S is the dielectrics contact area; more detail is provided in Figure S7 in the Supporting Information. Equation (2) implies the corresponding dependency of C_{max} on the relative permittivity, thus leading to variations in the output performance with the introduction of $BaTiO_3$ NPs to the PDMS, as evident in the empirical results shown in Figure 5.

To predict the possible electrostatic potential distributions concerning the relative permittivity modulations provided by the SIS, PDMS coating on the SIS layer, and PDMS/$BaTiO_3$ NP composite, simple finite-element simulations utilizing COMSOL Multiphysics are performed, as shown in **Figure 4**a–c. The simulation results indicate that the PDMS yields a higher electric potential than the SIS layer because of the larger electron affinity of the PDMS compared to that of the SIS elastomer (Figure 4b). The electric potential is further enhanced with increasing the relative permittivity of PDMS (ε_r = 2.8) by filling with $BaTiO_3$ NPs (Figure 4c); tetragonal $BaTiO_3$ has ε_r = 150 (Figure 4d). To further quantify the variation in the relative permittivity of the PDMS/$BaTiO_3$ composite versus changes in $BaTiO_3$ NP volume ratio between 0% and 60% (Figure 4e), a film-type capacitor is employed, where the accumulated charges (Q) are expressed as

$$Q = CV\left(1 - e^{-\frac{t}{RC}}\right) \quad (3)$$

In equation (3), C, V, t, and R are the capacitance, input voltage, charge time, and resistance, respectively.[35] Assuming that V is constant, C is calculated using the equation $C = \varepsilon_0\varepsilon_r A/d$, where ε_0, ε_r, A, and d are the permittivity of free space (8.854×10^{-12} F m^{-1}), the dielectric constant of the material, contact area (4 cm^2), and distance (30 μm) between the top and bottom electrodes, respectively. Increasing the $BaTiO_3$ NP volume ratio yields a linear increase in the relative permittivity for both theoretical and experimental results. This trend may be modeled as spherical composites in a continuous matrix, governed by Maxwell's equation[36]

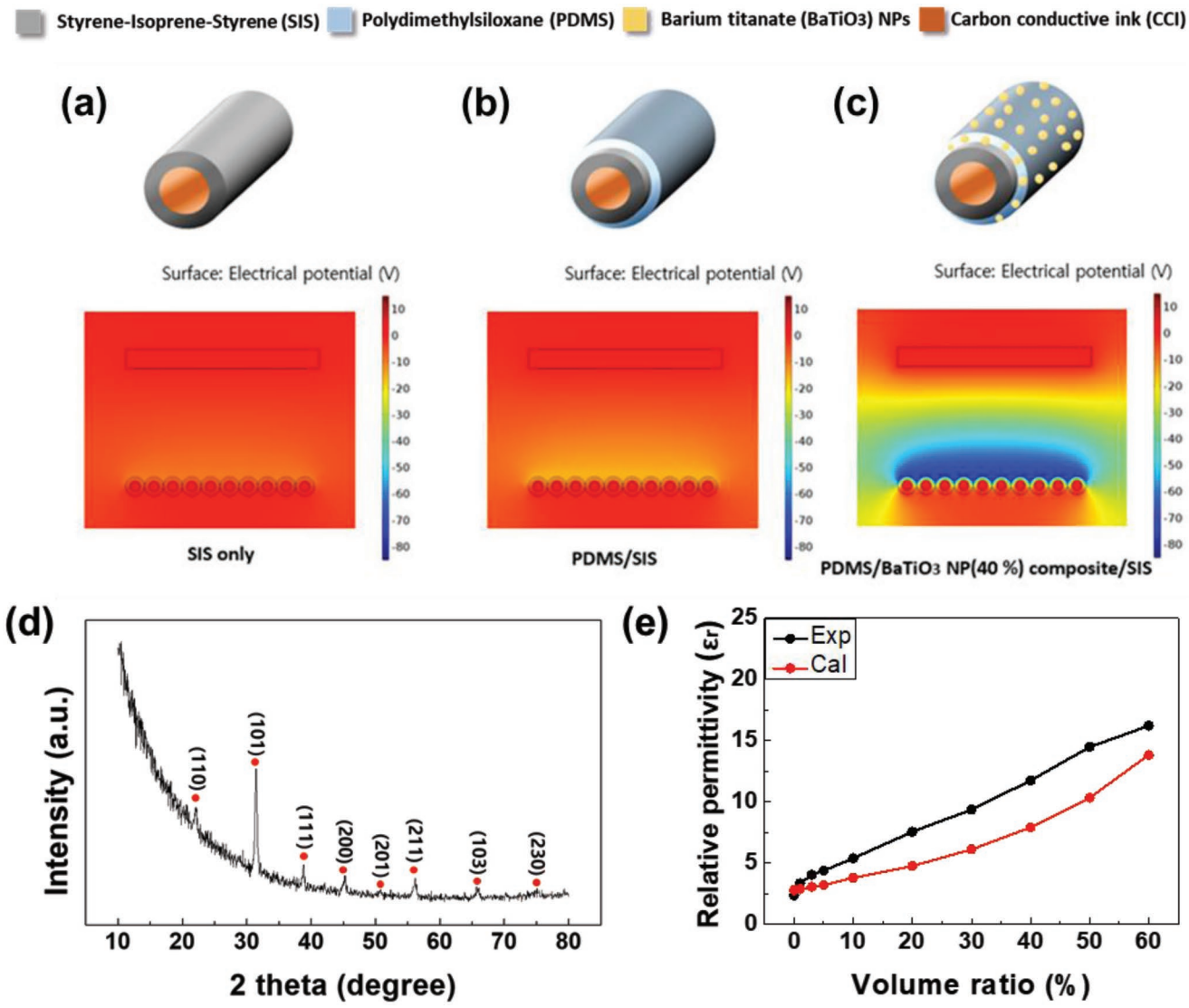

Figure 4. Finite-element simulations for the electrical potential distributions of the HS-TENG with three different surface configurations: a) bare SIS only, b) PDMS-coated SIS, and c) PDMS/40 vol% $BaTiO_3$ NP composite-coated SIS layer serving as the bottom plates, where the nylon 6-coated Ni–Cu flexible fabric is adopted as the top plate. d) Representative X-ray diffraction (XRD) patterns of tetragonal $BaTiO_3$ NPs used in the PDMS/$BaTiO_3$ NP composites. e) Relative permittivity variation versus $BaTiO_3$ NP volume ratio between 0% and 60%.

$$\varepsilon_{\text{eff}} = \varepsilon_1 \frac{\varepsilon_2 + 2\varepsilon_1 - 2(1-\varphi_1)(\varepsilon_1 - \varepsilon_2)}{\varepsilon_2 + 2\varepsilon_1 + (1-\varphi_1)(\varepsilon_1 - \varepsilon_2)} \quad (4)$$

In Equation (4), ε_1 and ε_2 are the relative permittivities of PDMS and $BaTiO_3$ NPs; φ_1 is the volume ratio of the PDMS matrix. As an example, the PDMS/$BaTiO_3$ NP composite with 40 vol% $BaTiO_3$ ($\varepsilon_1 = 2.8$, $\varepsilon_2 = 150$, $\varphi_1 = 0.6$) has the effective permittivity 7.91, where the actual experimental permittivity is 11.74. The experimental difference may correspond to the presence of nonhomogenously distributed $BaTiO_3$ NPs within the PDMS, as described later.

With the above structural observations and operation principle, the electrical signals generated by the HS-TENG are measured. **Figure 5**b,c shows the V_{OC} and I_{SC} of the HS-TENG, where the ten arrays of the HS 1D-CCT (4 cm in length) and nylon 6-coated Ni–Cu fabric serve as the bottom and top plates, respectively, with a contact area of 3×3 cm^2. In addition, bare SIS and various composites with 0–60 vol% $BaTiO_3$ NPs in the PDMS are tested for comparison. The bare SIS-based HS-TENG reveals the lowest output voltage of 17.1 V and current of 1.25 μA, while the PDMS-coated SIS-based HS TENG gives the output voltage of 18.8 V and current of 2.6 μA. Increasing the volume ratio of $BaTiO_3$ NPs leads to enhancements in the HS-TENG output performance, with the maximum output voltage of 76.7 V and current of 7.9 μA observed in the HS-TENG using the PDMS/$BaTiO_3$ composite containing 40 vol% $BaTiO_3$ NPs. With further increases in $BaTiO_3$ NP volume ratio, the output performance decreases. This decrease may suggest the presence of insufficient surface charge at interfaces in the composite by the formation of irregularly accumulated or distributed $BaTiO_3$ NPs at higher volume ratios. Closer observation of Figure 5a gives insight into the clear surface of

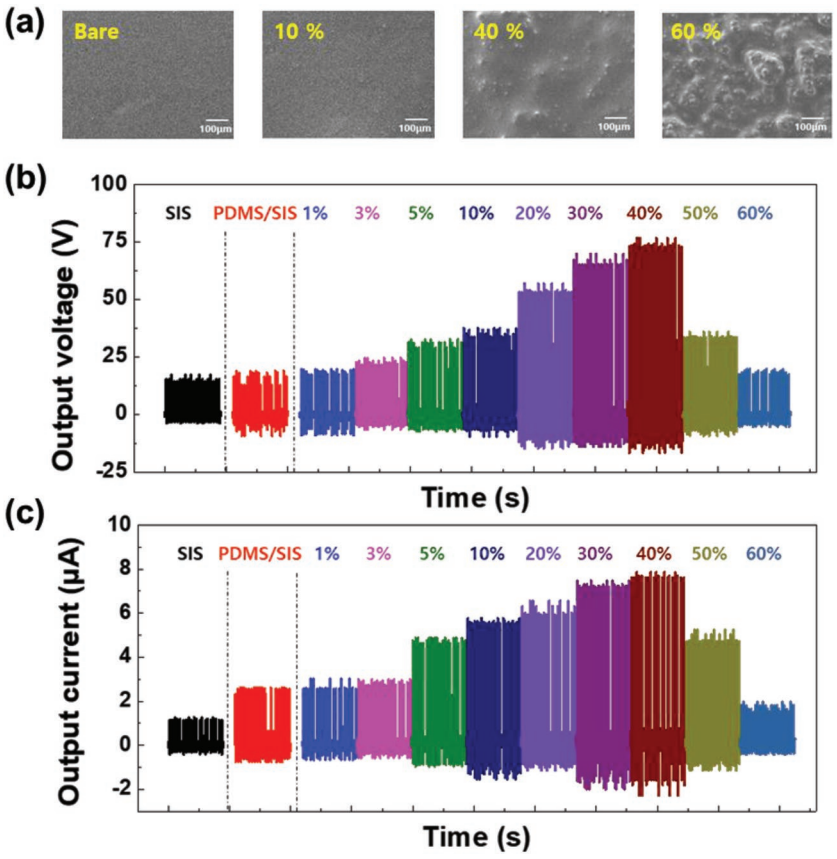

Figure 5. a) Top-view SEM images of the PDMS/$BaTiO_3$ NP composites with different volume ratios of $BaTiO_3$ NPs in the range 0–60%, where the PDMS/$BaTiO_3$ NP composites are coated on Si wafers for simple SEM analyses. Electrical responses of b) output voltage and c) current of the HS-TENG, where the 2D nylon 6-coated Ni–Cu fabric is used as the top plate. Maximum outputs of the HS-TENG are identified when the PDMS/$BaTiO_3$ NP composite uses 40 vol% $BaTiO_3$ NPs. The dominant contribution to the output performance may arise from the formation of proper nanostructured surfaces and the relatively high dielectric constants created by the optimized $BaTiO_3$ NP concentration in the bottom plate.

the PDMS/$BaTiO_3$ NP composite for volume ratios of ≤40%; volume ratios of >40% are linked to the possible formation of irregular interfacial surface charges via the nonuniform penetration or accumulation of large numbers of $BaTiO_3$ NPs in the PDMS.

The optimum HS-TENG, comprising an array of ten HS 1D-CCTs with the PDMS/40 vol% $BaTiO_3$ NP composite, is hereafter denoted Device A. To further characterize the human body motion-driven electricity production regarding a working frequency or compressive force in cyclic pressing, the output performance of Device A is recorded under various excitations, where the analyses are conducted at the external resistance of 10 MΩ or the constant force of 34 N. Figure S9a,b in the Supporting Information plots the frequency dependency in the output voltage and current of Device A. Increasing the frequency from 4 to 10 Hz increased the output voltage and current from 32.8 to 76 V and from 3.2 to 6.9 μA, respectively. Figure S9c,d in the Supporting Information reveals the compressive force dependency ranging from 8 to 68 N at 10 Hz, confirming clear increases in the output voltage and current from 64.7 to 117 V and 3.6 to 6.8 μA, respectively. In addition, since atmospheric humidity during the operation is one crucial factor that affects the electrical output of the Device A, the relative humidity (%RH)-dependent outputs of our device are exampled. As seen in Figure S10a,b in the Supporting Information, a higher humidity condition has a negatively significant impact on the device performance possibly owing to the neutralization effect on the generated triboelectric surface charges by the humidity.

To determine the applicability of the HS-TENG as an element of wearable devices, the electrical output performance of Device A is recorded under uniaxial stretching states at several strains, where the electrical outputs of Device A are taken at the compressive force of 34 N and frequency of 10 Hz. **Figure 6**a shows the representative optical images of Device A at the initial and stretched states, illustrating the undistorted stretchability from 0% to 250% even after recovery from the stretched states. Strain contributions to the output performance are given in Figure 6b,c, demonstrating a slight decrease in the output voltage and current from 76 to 34.5 V and from 7.6 to 3.1 μA, respectively, with increasing strain. Usually, such trends created by stretching (corresponding to the degradation of the HS-TENG in our work) mainly arise from reductions in the effective surface contact areas for charge transfer between the stretched HS 1D-CCT and the Nylon 6-coated Ni–Cu fabric. Table S1 in the Supporting Information provides experimental proof of the variations in cross-sectional diameters of the HS 1D-CCT under applied strain. The most prominent feature is the similarity in electrical output even after recovery from the stretched states; no distinct degradation in output performance is observed regardless of applied strain when compared to that of the initial state.

To demonstrate the HS-TENG as a plausible component of various wearable applications, the external load-dependent output characteristics of Device A are examined at compressive force of 34 N and frequency of 10 Hz. Figure S11a in the Supporting Information depicts the output voltage and current as a function of external load resistance. Increasing the load resistance from 1 to 10^3 MΩ induces an increase in voltage from 12.1 to 153.4 V and a decrease in current from 15.8 to 0.3 μA, respectively. The corresponding instantaneous average power density is shown in Figure S11b in the Supporting Information; the maximum output power of 360.4 μW occurs at a load of 10 MΩ. The output power density is approximately determined by the contact area of 6 cm^2. The plot of output power density versus the $BaTiO_3$ NPs volume ratio confirms the expected maximum value in Device A (200.9 μW cm^{-2}), as evident in Figure S11c in the Supporting Information. The mechanical stability for the Device A is also tested with a homemade

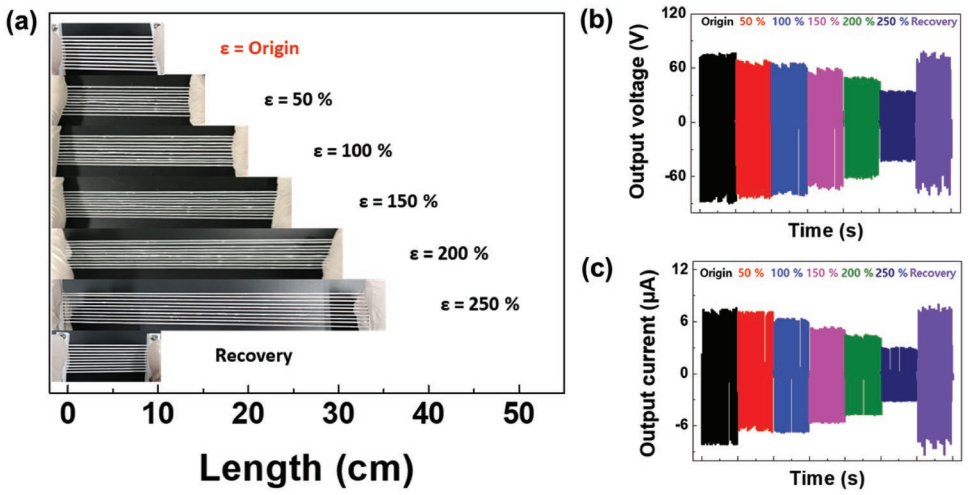

Figure 6. a) Optical images of arrays of 10 HS 1D-CCTs at initial and stretched states, where the HS 1D-CCT contains the PDMS/$BaTiO_3$ NP (40 vol%) composites. b) Output voltage and c) current of Device A under various tensile strains, clearly demonstrating the relatively small influence on the outputs by applied strains, even after recovery to the initial state.

pushing machine (Figure S12, Supporting Information). The consecutive cyclic response of 3000 cycles supports the distinct mechanical robustness and stable endurance without exhibiting significant degradation. However, the variation on the surface geometrics of PDMS/$BaTiO_3$ layers under higher consecutive impacts as one degradation example is given in Figure S13 in the Supporting Information.

To determine the effective electrical accommodation arising from the complex deformations generated by human body motion, a loom textile weaving approach is adapted to prepare a woven HS-TENG textile (denoted Textile A), along with a full-bridge rectifier circuit for an ordered arrangement of the output signals. Figure S14a in the Supporting Information shows a simple photograph of Textile A; Figure S14c,d in the Supporting Information reveals the average output voltage and current of ≈278 V and ≈27.5 μA taken at compressive force of 34 N and frequency of 10 Hz, where the Nylon 6-coated Ni–Cu fabric (3×3 cm^2) is used as a top plate. Textile A is used to operate 100 serially connected red commercial LEDs without using any capacitor (Figure S14b, Supporting Information). Figure S15a–f in the Supporting Information shows photographs of Textile A under various strains, still demonstrating inherently robust stretchability up to 250% strain, as expected.

Because textile durability and stability are crucial for wearable device applications, as are efficient and high energy generation, the electrical performance of the larger Textile A (6×5 cm^2) is recorded under various harsh conditions, including folded, stretched, and washed states. **Figure 7**a–d shows the representative optical images of Textile A under folding, twisting, 100% stretching, and completely drying states after 30 min washing, respectively. Their corresponding outputs over 100 consecutive cycles are shown in Figure 7e,f, where the analyses are conducted at the same compressive force of 34 N and frequency of 10 Hz. No degradation in electrical characteristics occurs,

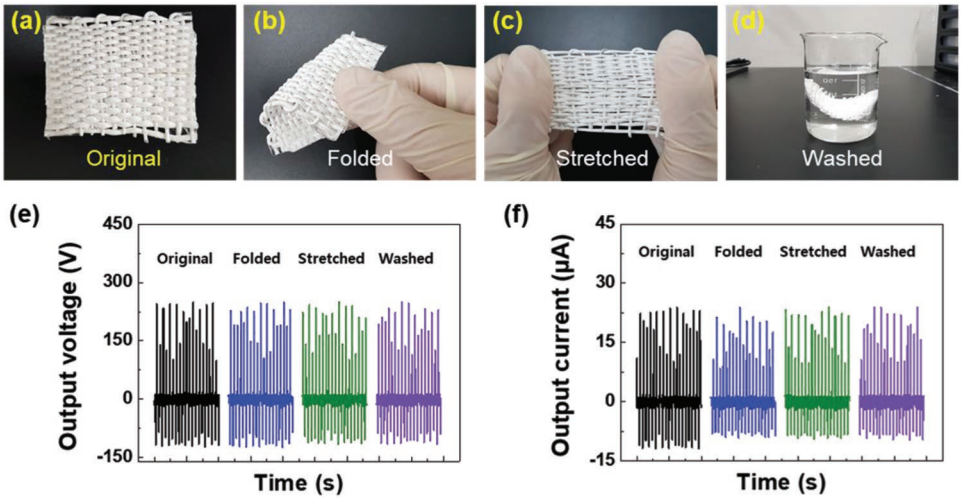

Figure 7. Electrical stability test of Textile A under three different extreme conditions. Photographs of a) original, b) folded, c) stretched, and d) washed states. e) Output voltages and f) currents after experiencing extreme conditions, demonstrating highly reliable and stable output features without critical variations in electrical performance.

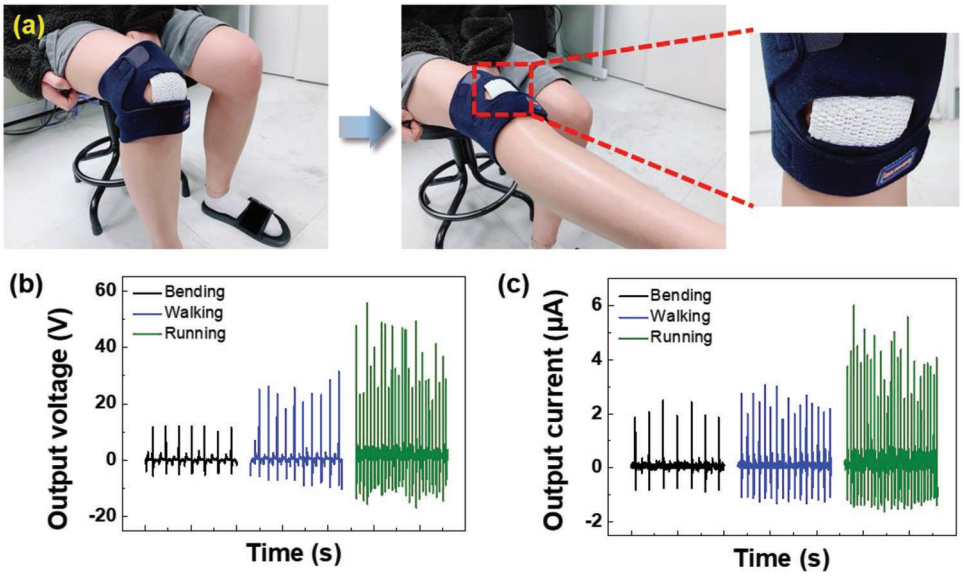

Figure 8. a) Photographs of Textile A integrated on the human knee protector as a wearable human motion-driven self-powered system. b) Output voltages and c) currents of Textile A under human bending (black), walking (blue), and running (green) motions.

demonstrating high durability and stability. The observed reliability is mainly associated with the uniformly dispersed PDMS/$BaTiO_3$ composite coating on the SIS, reflecting robust protection, and water resistance under various extreme conditions.

As a prototype wearable energy harvester based on human motion, Textile A is integrated in a wrap for the human knee, designed to experience external stress caused by the irregular and nonuniform bending, walking, and running motions of the human knee. **Figure 8** depicts photographs and the corresponding output performance of the knee wrap. An instantaneous output voltage of 12.1 V and current of 2.5 μA is achieved under bending knee motion at an angle of ≈90° and a frequency of 0.7 Hz. Increasing the frequency to 1.1 Hz (walking) increases the output voltage to 31.5 V and the current to 3.1 μA. At the frequency of 2.7 Hz (running), the output voltage of 55.6 V and current of 6 μA are obtained. With the frequency of walking of about 1.5 times that of the bending motion, the output voltage and current are enhanced by 2.6 times and 1.24 times, respectively. Similarly, the output voltage and current of running are 4.6 times and 2.4 times higher than those of bending. Thus, use of the above stretchable textile enables the suitable generation of energy by diverse human motions.

3. Conclusion

In summary, we introduce a 1D thread-based HS-TENG based on lab-made intrinsically stretchable SIS tubes with CCI as a core electrode; the HS 1D-CCT remains conductive under stretching up to 250%. The precise modulation of relative permittivity by manipulating the content of PDMS/$BaTiO_3$ NP composite coatings on the SIS yields a strong enhancement in the output performance recorded in the vertical-contact mode, where the outputs are commonly ascribed to the triboelectric effect and charge induction. The outstanding output performance of HS-TENGs textiles created by weaving is retained even under various extremely harsh conditions, including folding, twisting, and washing. Furthermore, the HS-TENG has a significant advantage of introducing a high compatibility that may be used in the future real textile industry, possibly contributing to the proliferation of wearable electronic devices (Table S2, Supporting Information).

4. Experimental Section

Fabrication of Nylon 6-Coated Ni–Cu Fabric: Before fabrication, the Ni–Cu fabric was sequentially cleaned with acetone, ethanol, and deionized water for 15 min each, respectively, to remove possible residues. Nylon 6 (polycaprolactam, Sigma-Aldrich) was mixed with formic acid (American chemical society (ACS) reagent, Sigma-Aldrich) at the weight ratio of 10:1, and the mixture was stirred at 60 °C for 6 h. After dissolving, the solution was spin coated at 3000 rpm for 30 s (ACE-200, iNexus). Finally, a uniform nylon 6 film coated on Ni–Cu fabric was obtained by cooling in air.

Fabrication of HS 1D-CCT: Highly stretchable coaxial fibers were manufactured using a thermal extrusion machine (Desktop filament extruder, Wellzoom). At the outlet of the extruder, a nozzle (27 G stainless steel, diameter 0.406 mm) was installed. The coaxial structure of the SIS elastomer (poly[styrene-*b*-isoprene-*b*-styrene], Sigma-Aldrich) was achieved using the extruder with the internal temperature of 220 °C and nozzle temperature of 210 °C, utilizing an 0.35 mm metal thread as a mold at the spinning rate of 40 mm min^{-1}. To enhance the output performance, $BaTiO_3$ NPs (barium titanate(IV), Sigma-Aldrich) with an average size of 100 nm were mixed with PDMS (ELASTOSIL E43, WACKER) at the optimal volume ratio of 40%. A hexane (*n*-hexane, Sigma-Aldrich) solution was added to uniformly blend the $BaTiO_3$ NPs and PDMS and to control the viscosity of the composite, ensuring uniform coating of the coaxial structure of the SIS elastomer. The volume ratio of PDMS to hexane was 1:1. After mixing uniformly, the mixture was poured over the prefabricated SIS elastomer-coated metal thread. When fully solidified naturally at room temperature, the cured elastomer was peeled off from the metal thread. Subsequently, CCI (Premium Carbon Conductive Grease, MG Chemicals) was injected into the cavity using a syringe. Finally, a Cu lead wire attached on one side for electrical connection and both ends of the coaxial fiber were sealed by injecting conductive ink and applying the thermal compression method.

Electrical Measurement: The electrical output responses of the HS-TENGs were measured with a mechanical linear motor (E1100, Linmot), an oscilloscope (WavePro 735Zi, Lecroy), and a low-noise current amplifier (SR570, Standard Research System) at various frequencies. The relative permittivities of the PDMS and PDMS/$BaTiO_3$ composites were ascertained using a digital multimeter (388A, B&K Precision). The dynamic mechanical behavior of the HS 1D-CCTs was measured by a tensile testing machine (TD-U01, TnDorf) at room temperature. The crystalline structure of the $BaTiO_3$ NPs was characterized with an X-ray diffraction (SmartLab, Rigaku) system. In addition, FE-SEM (S-4800, Hitachi) analysis was performed to observe the surface morphologies of the PDMS/$BaTiO_3$ composite layers.

Supporting Information

Supporting Information is available from the Wiley Online Library or from the author.

Acknowledgements

J.K. and W.K. contributed equally to this work. This research was supported in part by Korea Electric Power Corporation (Grant No. R18XA06-08) and National Research Foundation of Korea (Grant No. NRF-2019M3F3A1A03079422).

Conflict of Interest

The authors declare no conflict of interest.

Keywords

1D poly[styrene-*b*-isoprene-*b*-styrene] tube, carbon conductive ink, high dielectric permittivity, stretchable triboelectric nanogenerators, woven textiles

Received: October 1, 2019
Revised: November 16, 2019
Published online: December 17, 2019

[1] X. Pu, W. Song, M. Liu, C. Sun, C. Du, C. Jiang, X. Huang, D. Zou, W. Hu, Z. L. Wang, *Adv. Energy Mater.* **2016**, *6*, 1601048.
[2] M. Kanik, M. G. Say, B. Daglar, A. F. Yavuz, M. H. Dolas, M. M. El-Ashry, M. Bayindir, *Adv. Mater.* **2015**, *27*, 2367.
[3] S. S. Kwak, H.-J. Yoon, S.-W. Kim, *Adv. Funct. Mater.* **2019**, *29*, 1804533.
[4] H. Kim, S. M. Kim, H. Son, H. Kim, B. Park, J. Ku, J. I. Sohn, K. Im, J. E. Jang, J.-J. Park, O. Kim, S. Cha, Y. J. Park, *Energy Environ. Sci.* **2012**, *5*, 8932.
[5] Q. Zhang, Y. Wang, E. S. Kim, *J. Microelectromech. Syst.* **2015**, *24*, 1193.
[6] A. Bibo, R. Masana, A. King, G. Li, M. F. Daqaq, *Phys. Lett. A* **2012**, *376*, 2163.
[7] Z. L. Wang, J. Song, *Science* **2006**, *312*, 242.
[8] R. Yang, Y. Qin, C. Li, G. Zhu, Z. L. Wang, *Nano Lett.* **2009**, *9*, 1201.
[9] C. R. Bowen, J. Taylor, E. LeBoulbar, D. Zabek, A. Chauhan, R. Vaish, *Energy Environ. Sci.* **2014**, *7*, 3836.
[10] Y. Yang, W. Guo, K. C. Pradel, G. Zhu, Y. Zhou, Y. Zhang, Y. Hu, L. Lin, Z. L. Wang, *Nano Lett.* **2012**, *12*, 2833.
[11] M.-L. Seol, S.-B. Jeon, J.-W. Han, Y.-K. Choi, *Nano Energy* **2017**, *31*, 233.
[12] Y. Zi, H. Guo, Z. Wen, M.-H. Yeh, C. Hu, Z. L. Wang, *ACS Nano* **2016**, *10*, 4797.
[13] M.-F. Lin, J. Xiong, J. Wang, K. Parida, P. S. Lee, *Nano Energy* **2018**, *44*, 248.
[14] Z. Tian, J. He, X. Chen, T. Wen, C. Zhai, Z. Zhang, J. Cho, X. Chou, C. Xue, *RSC Adv.* **2018**, *8*, 2950.
[15] R. I. Haque, P.-A. Farine, D. Briand, *Proceedings* **2017**, *1*, 580.
[16] T. Zhao, J. Li, H. Zeng, Y. Fu, H. He, L. Xing, Y. Zhang, X. Xue, *Nanotechnology* **2018**, *29*, 405504.
[17] D. Kim, S.-J. Park, S.-B. Jeon, M.-L. Seol, Y.-K. Choi, *Adv. Electron. Mater.* **2016**, *2*, 1500331.
[18] J. J. Shao, W. Tang, T. Jiang, X. Y. Chen, L. Xu, B. D. Chen, T. Zhou, C. R. Deng, Z. L. Wang, *Nanoscale* **2017**, *9*, 9668.
[19] J. Chun, B. U. Ye, J. W. Lee, D. Choi, C.-Y. Kang, S.-W. Kim, Z. L. Wang, J. M. Baik, *Nat. Commun.* **2016**, *7*, 12985.
[20] M. Xu, P. Wang, Y.-C. Wang, S. L. Zhang, A. C. Wang, C. Zhang, Z. Wang, X. Pan, Z. L. Wang, *Adv. Energy Mater.* **2018**, *8*, 1702432.
[21] D. Y. Kim, H. S. Kim, D. S. Kong, M. Choi, H. B. Kim, J.-H. Lee, G. Murillo, M. Lee, S. S. Kim, J. H. Jung, *Nano Energy* **2018**, *45*, 247.
[22] K. Dong, X. Peng, Z. L. Wang, *Adv. Mater.* **2019**, 1902549.
[23] K. Dong, J. Deng, Y. Zi, Y.-C. Wang, C. Xu, H. Zou, W. Ding, Y. Dai, B. Gu, B. Sun, Z. L. Wang, *Adv. Mater.* **2017**, *29*, 1702648.
[24] W. Seung, M. K. Gupta, K. Y. Lee, K.-S. Shin, J.-H. Lee, T. Y. Kim, S. Kim, J. Lin, J. H. Kim, S.-W. Kim, *ACS Nano* **2015**, *9*, 3501.
[25] S. Wang, M. He, B. Weng, L. Gan, Y. Zhao, N. Li, Y. Xie, *Nanomaterials* **2018**, *8*, 657.
[26] W. B. Ko, D. S. Choi, C. H. Lee, J. Y. Yang, G. S. Yoon, J. P. Hong, *Adv. Mater.* **2017**, *29*, 1704434.
[27] D. Choi, S. Yang, C. Lee, W. Kim, J. Kim, J. Hong, *ACS Appl. Mater. Interfaces* **2018**, *10*, 33221.
[28] R. Sinclair, *Textiles and Fashion*, Woodhead Publishing, Sawston, UK **2015**.
[29] B. D. Opell, D. Jain, A. Dhinojwala, T. A. Blackledge, *J. Exp. Biol.* **2018**, *221*, jeb161539.
[30] S. Matsusaka, H. Maruyama, T. Matsuyama, M. Ghadiri, *Chem. Eng. Sci.* **2010**, *65*, 5781.
[31] G. S. P. Castle, *J. Electrost.* **1997**, *40–41*, 13.
[32] J. Lowell, A. C. Rose-Innes, *Adv. Phys.* **1980**, *29*, 947.
[33] S. Niu, S. Wang, L. Lin, Y. Liu, Y. S. Zhou, Y. Hu, Z. L. Wang, *Energy Environ. Sci.* **2013**, *6*, 3576.
[34] J. Chen, H. Guo, X. He, G. Liu, Y. Xi, H. Shi, C. Hu, *ACS Appl. Mater. Interfaces* **2016**, *8*, 736.
[35] J. W. Lee, H. J. Cho, J. Chun, K. N. Kim, S. Kim, C. W. Ahn, I. W. Kim, J.-Y. Kim, S.-W. Kim, C. Yang, J. M. Baik, *Sci. Adv.* **2017**, *3*, e1602902.
[36] D.-H. Yoon, J. Zhang, B. I. Lee, *Mater. Res. Bull.* **2003**, *38*, 765.

